An Artificial Molecular Switch that Mimics the Visual Pigment and Completes its Photocycle in Picoseconds

Adalgisa Sinicropi[§], Elena Martin[¢], Mikhail Ryasantsev[¶], Jan Helbing[*], Julien Briand[+], Divya Sharma[+], Jérémie Léonard[+], Stefan Haacke[+], Andrea Cannizzo[†], Majed Chergui[†], Vinicio Zanirato[#], Stefania Fusi[§], Fabrizio Santoro[#], Riccardo Basosi[§], Nicolas Ferré[‡] and Massimo Olivucci[§,¶]

[§] Dipartimento di Chimica, Università di Siena, via Aldo Moro 2, I-53100 Siena, Italy. [¶] Chemistry Department, Bowling Green State University, Bowling Green 43403, OH. [¢] Departamento de Ingeniería Química y Química Física Universidad de Extremadura Avenida de Elvas s/n Badajoz 06071 España. [*] Physikalisch-Chemisches Institut, Universität Zürich, Winterthurerstrasse 190, 8057 Zürich, Switzerland. [†] Laboratoire de Spectroscopie Ultrarapide, Ecole Polytechnique Fédérale de Lausanne, CH-1015 Lausanne-Dorigny, Switzerland. [#] Dipartimento di Scienze Farmaceutiche, Università di Ferrara, via Fossato di Mortara 17-19, I-44100 Ferrara, Italy. [#] Istituto per i Processi Chimico-Fisici del CNR, Via Moruzzi 1, I-56124 Pisa, Italy. [‡] Laboratoire de Chimie Théorique et de Modélisation Moléculaire, UMR 6517-CNRS Université de Provence, Case 521 – Faculté de Saint-Jérôme, Av. Esc. Normandie Niemen, 13397 Marseille Cedex 20, France.

Supporting Information Appendix

An extended version of the present *Supporting Information Appendix* (115 pages) featuring the compelet set of structural data (Cartesian coordinates) is available by contacting the last corresponding author at: olivucci@unisi.it

1. Computations

The model of the switches in solution was constructed by placing the chromophore in a rectangular box of methanol molecules positioned within 10 Å from any given atom of the chromophore using xleap module of Amber package (1). To neutralize the system we added a chloride anion. The average ground state configuration of the methanol molecules (i.e. the solvent) has been determined according to the following procedure: the solvent (including the counterion) was minimized for 2000 steps using the steepest descent method while keeping the chromophore (i.e. the solute) fixed in its gas-phase configuration. In this step the partial charges of the chromophore atoms were determined with GAUSSIAN03(2), using a Restrained ElectroStatic Potential (RESP) procedure at the HF/6-31G* level of theory. In the next step we performed CASSCF/6-31G*/AMBER geometry optimization to relax the coordinates of the QM chromophore, MM counterion and solvent molecules (only in the case of data in next Section 1) with any atom within less than 4.5 Å from any solute atom. The positions of the remaining solvent molecules, more distant from the chromophore, were kept frozen. The QM calculations are based on a CASSCF/6-31G* level including an active space of 12 electrons in 11 π-orbitals (i.e. the full π-system of the solute). The MM (we use the Amber96 force field) and QM parts interact in the following way: (i) the QM atoms feel the set of MM point charges, (ii) stretching, bending and torsional potentials involving at least one MM atom are described by the MM

potential (iii) QM and MM atom pairs interact via either standard or re-parametrized van der Waals potentials. Since the van der Waals atomic parameters for the switch molecule are not defined in the Amber96 force-field, we have used the parameters already developed in ref. (3) following the procedure proposed in ref. (4). The van der Waals parameters are (R*=1.8778 Å, ε=0.0860 kcal·mol^{-1}) for a sp2 carbon atom of the switch model system, (R*=1.8891 Å, ε=0.1094 kcal·mol^{-1}) for a sp3 carbon atom of 1 system and (R*=0.9237 Å, ε=0.0157 kcal.mol^{-1}) for the hydrogen atoms attached to sp2 or sp3 carbons. The van der Waals parameters for the nitrogen atom are (R*=1.8311 Å, ε=0.1700 kcal·mol^{-1}) and for the hydrogen atom bounded to it are (R*=0.6024 Å, ε=0.0157 kcal·mol^{-1}). The van der Waals parameters for the oxygen atom of the p-OMe group have been taken from the general Amber force field (GAFF) (5) for organic molecules and are (R*=1.6837 Å, ε=0.1700 kcal·mol^{-1}). GAFF is designed to be compatible with existing Amber force fields for proteins and nucleic acids, and has parameters for most organic and pharmaceutical molecules that are composed of H, C, N, O, S, P, and halogens. CASSCF/6-31G*/AMBER geometry optimization is carried out with the GAUSSIAN03(2), TINKER 4.2 (6). To account for a dynamical correlation energy a CASPT2 on four root state average CASSCF calculations (weights: 0.25, 0.25, 0.25, 0.25) were carried out using the MOLCAS 6.2 (7) software.). The accuracy of this (low-cost) solvent model is assessed re-optimizing the Z-**1** and E-**1** equilibrium structures using the ASEP/MD protocol (see Section 4 below) that provides a rigorous model of the solvent shell. This is a mean field approximation (8) method where solvent MM-based molecular dynamics calculations and solute QM geometry optimizations are alternated and iterated until the solute charge distribution and the average electrostatic potential generated by the solvent are mutually equilibrated.

2. Z to E and E to Z paths

Table S2.1 Absolute energy (hartee) for the Z-**1** (relaxed and fixed solvent shell) and E-**1** (relaxed solvent shell) optimized structures[a] along the $C_{9'}$-$C_{1'}$-C_4-C_5 reaction coordinate.

Structure (Z-1) Relaxed Solvent Shell	***Energy***	
	CASSCF	***CASPT2***
[b]S_0-Z-1 ($S_0 \rightarrow S_1$)	-786.60980 (S_0)	-788.43750 (S_0)
S_0-Z-1 ($S_0 \rightarrow S_2$)	MM: -0.65990	-788.31650 (S_1)
S_0-Z-1 ($S_0 \rightarrow S_3$)		-788.29464 (S_2)
		-788.25216 (S_3)
S_1-17deg ($S_0 \rightarrow S_1$)	-786.56463 (S_0)	-788.41552 (S_0)
	-786.45068 (S_1)	-788.32874 (S_1)
S_1-17deg ($S_0 \rightarrow S_2$)	MM: -0.66651	-788.28558 (S_2)
S_1-17deg ($S_0 \rightarrow S_3$)		-788.27459 (S_3)
S_1-22deg ($S_0 \rightarrow S_1$)	-786.56382 (S_0)	-788.41509 (S_0)
	-786.45292 (S_1)	-788.33084 (S_1)
S_1-22deg ($S_0 \rightarrow S_2$)	MM: -0.66642	-788.28577 (S_2)
S_1-22deg ($S_0 \rightarrow S_3$)		-788.27596 (S_3)

S_1-33deg ($S_0 \rightarrow S_1$)	-786.56073 (S_0) -786.45742 (S_1)	-788.41240 (S_0) -788.33449 (S_1) -788.28409 (S_2) -788.27621 (S_3)
S_1-33deg ($S_0 \rightarrow S_2$)	MM: -0.66675	
S_1-33deg ($S_0 \rightarrow S_3$)		
S_1-41deg ($S_0 \rightarrow S_1$)	-786.55691 (S_0) -786.46535 (S_1)	-788.40999 (S_0) -788.34277 (S_1) -788.28229 (S_2) -788.27286 (S_3)
S_1-41deg ($S_0 \rightarrow S_2$)	MM: -0.66560	
S_1-41deg ($S_0 \rightarrow S_3$)		
S_1-49deg ($S_0 \rightarrow S_1$)	-786.55246 (S_0) -786.47428 (S_1)	-788.40598 (S_0) -788.35229 (S_1) -788.27964 (S_2) -788.27287 (S_3)
S_1-49deg ($S_0 \rightarrow S_2$)	MM: -0.66532	
S_1-49deg ($S_0 \rightarrow S_3$)		
S_1-57deg ($S_0 \rightarrow S_1$)	-786.54529 (S_0) -786.48351 (S_1)	-788.39926 (S_0) -788.36052 (S_1) -788.27464 (S_2) -788.26790 (S_3)
S_1-57deg ($S_0 \rightarrow S_2$)	MM: -0.66522	
S_1-57deg ($S_0 \rightarrow S_3$)		
S_1-65deg ($S_0 \rightarrow S_1$)	-786.53608 (S_0) -786.49291 (S_1)	-788.389212 (S_0) -788.36758 (S_1) -788.26797 (S_2) -788.26343 (S_3)
S_1-65deg ($S_0 \rightarrow S_2$)	MM: -0.66554	
S_1-65deg ($S_0 \rightarrow S_3$)		
S_1-73deg ($S_0 \rightarrow S_1$)	-786.52585 (S_0) -786.50295 (S_1)	-788.37682 (S_0) -788.37340 (S_1) -788.26050 (S_2) -788.26333 (S_3)
S_1-73deg ($S_0 \rightarrow S_2$)	MM: -0.66549	
S_1-73deg ($S_0 \rightarrow S_3$)		
S_1-81deg ($S_0 \rightarrow S_1$)	-786.52171 (S_0) -786.51920 (S_1)	-788.38141 (S_0) -788.37588 (S_1) -788.26579 (S_2) -788.27113 (S_3)
S_1-81deg ($S_0 \rightarrow S_1$)	MM: -0.66407	
S_1-81deg ($S_0 \rightarrow S_2$)		
S_1-90deg ($S_0 \rightarrow S_1$)	-786.51520(S_0) -786.50683 (S_1)	-788.36486 (S_0) -788.36898 (S_1)

S_1-90deg ($S_0 \rightarrow S_1$)	MM: -0.66694	-788.25492 (S_2) -788.25965 (S_3)
S_1-90deg ($S_0 \rightarrow S_2$)		

Structure (E-1) Relaxed Solvent Shell	***Energy***	
	CASSCF	***CASPT2***
$^{c}S_0$-E-1 ($S_0 \rightarrow S_1$)	-786.54677 (S_0)	-788.44039 (S_0) -788.31807 (S_1) -788.29266 (S_2) -788.25170 (S_3)
S_0-E-1 ($S_0 \rightarrow S_2$)	MM: -0.59677	
S_0-E-1 ($S_0 \rightarrow S_3$)		
S_1-E-165deg ($S_0 \rightarrow S_1$)	-786.51209 (S_0) -786.40073 (S_1)	-788.40920 (S_0) -788.32560 (S_1) -788.27543 (S_2) -788.27195 (S_3)
S_1-E-165deg ($S_0 \rightarrow S_2$)	MM: -0.62288	
S_1-E-165deg ($S_0 \rightarrow S_3$)		
S_1-E-157deg ($S_0 \rightarrow S_1$)	-786.50700 (S_0) -786.40174 (S_1)	-788.40530 (S_0) -788.32672 (S_1) -788.27289 (S_2) -788.27100 (S_3)
S_1-E-157deg ($S_0 \rightarrow S_2$)	MM: -0.62258	
S_1-E-157deg ($S_0 \rightarrow S_3$)		
S_1-E-146deg ($S_0 \rightarrow S_1$)	-786.50459 (S_0) -786.40536 (S_1)	-788.41209 (S_0) -788.33991 (S_1) -788.28286 (S_2) -788.28547 (S_3)
S_1-E-146deg ($S_0 \rightarrow S_2$)	MM: -0.61080	
S_1-E-146deg ($S_0 \rightarrow S_3$)		
S_1-E-134deg ($S_0 \rightarrow S_1$)	-786.49627 (S_0) -786.41127 (S_1)	-788.40504 (S_0) -788.34785 (S_1) -788.27677 (S_2) -788.27824 (S_3)
S_1-E-134deg ($S_0 \rightarrow S_2$)	MM: -0.61025	
S_1-E-134deg ($S_0 \rightarrow S_3$)		
S_1-E-124deg ($S_0 \rightarrow S_1$)	-786.48906 (S_0) -786.42121 (S_1)	-788.39774 (S_0) -788.35533 (S_1) -788.27276 (S_2) -788.27153 (S_3)
S_1-E-124deg ($S_0 \rightarrow S_2$)	MM: -0.61143	
S_1-E-124deg ($S_0 \rightarrow S_3$)		
S_1-E-114deg ($S_0 \rightarrow S_1$)	-786.47998 (S_0) -786.43139 (S_1)	-788.38874 (S_0) -788.36318 (S_1) -788.26664 (S_2) -788.26588 (S_3)
S_1-E-114deg ($S_0 \rightarrow S_2$)	MM: -0.61191	
S_1-E-114deg ($S_0 \rightarrow S_3$)		
S_1-E-106deg ($S_0 \rightarrow S_1$)	-786.47765 (S_0) -786.44758 (S_1)	-788.37589 (S_0) -788.36671 (S_1)

S_1-E-106deg ($S_0 \rightarrow S_2$)	MM: -0.62010	-788.25835 (S_2) -788.26070 (S_3)
S_1-E-106deg ($S_0 \rightarrow S_3$)		
S_1-E-96deg ($S_0 \rightarrow S_1$)	-786.48274 (S_0) -786.47288 (S_1)	-788.36735 (S_0) -788.37861 (S_1)
S_1-E-96deg ($S_0 \rightarrow S_2$)	MM: -0.62785	-788.26067 (S_2)
S_1-E-96deg ($S_0 \rightarrow S_3$)		-788.26497 (S_3)
S_1-E-92deg ($S_0 \rightarrow S_1$)	-786.47982(S_0) -786.47900 (S_1)	-788.36907 (S_0) -788.37980 (S_1)
S_1-E-92deg ($S_0 \rightarrow S_2$)	MM: -0.62871	-788.26041 (S_2)
S_1-E-92deg ($S_0 \rightarrow S_3$)		-788.26456 (S_3)

Structure (Z-1) Fixed [d] ***Solvent Shell***	***Energy***	
	CASSCF	***CASPT2***
S_1-17deg ($S_0 \rightarrow S_1$)	-785.91544 (S_0) -785.80087 (S_1)	-788.41716 (S_0) -788.33087 (S_1)
S_1-17deg ($S_0 \rightarrow S_2$)	MM: -0.01596	-788.28629 (S_2)
S_1-17deg ($S_0 \rightarrow S_3$)		-788.27721 (S_3)
S_1-22deg ($S_0 \rightarrow S_1$)	-785.91413 (S_0) -785.80312 (S_1)	-788.41581 (S_0) -788.33218 (S_1)
S_1-22deg ($S_0 \rightarrow S_2$)	MM: -0.01635	-788.28578 (S_2)
S_1-22deg ($S_0 \rightarrow S_3$)		-788.27797 (S_3)
S_1-33deg ($S_0 \rightarrow S_1$)	-785.91070 (S_0) -785.80763 (S_1)	-788.41229 (S_0) -788.33497 (S_1)
S_1-33deg ($S_0 \rightarrow S_2$)	MM: -0.01705	-788.28369 (S_2)
S_1-33deg ($S_0 \rightarrow S_3$)		-788.27753 (S_3)
S_1-41deg ($S_0 \rightarrow S_1$)	-785.90660 (S_0) -785.81561 (S_1)	-788.40850 (S_0) -788.34181 (S_1)
S_1-41deg ($S_0 \rightarrow S_2$)	MM: -0.01736	-788.28108 (S_2)
S_1-41deg ($S_0 \rightarrow S_3$)		-788.27611 (S_3)
S_1-49deg ($S_0 \rightarrow S_1$)	-785.90226 (S_0) -785.82476 (S_1)	-788.40388 (S_0) -788.35091 (S_1)
S_1-49deg ($S_0 \rightarrow S_2$)	MM: -0.01763	-788.27754 (S_2)
S_1-49deg ($S_0 \rightarrow S_3$)		-788.27176 (S_3)

S_1-57deg ($S_0 \rightarrow S_1$)	-785.89593 (S_0) -785.83428 (S_1)	-788.39701 (S_0) -788.35837 (S_1) -788.27250 (S_2) -788.26670 (S_3)
S_1-57deg ($S_0 \rightarrow S_2$)	MM: -0.01823	
S_1-57deg ($S_0 \rightarrow S_3$)		
S_1-65deg ($S_0 \rightarrow S_1$)	-785.88704 (S_0) -785.84409 (S_1)	-788.38713 (S_0) -788.36538 (S_1) -788.26596 (S_2) -788.26253 (S_3)
S_1-65deg ($S_0 \rightarrow S_2$)	MM: -0.01862	
S_1-65deg ($S_0 \rightarrow S_3$)		
S_1-73deg ($S_0 \rightarrow S_1$)	-785.87663 (S_0) -785.85440 (S_1)	-788.37400 (S_0) -788.37085 (S_1) -788.25829 (S_2) -788.26100 (S_3)
S_1-73deg ($S_0 \rightarrow S_2$)	MM: -0.01892	
S_1-73deg ($S_0 \rightarrow S_3$)		
S_1-81deg ($S_0 \rightarrow S_1$)	-785.86536 (S_0) -785.86457 (S_1)	-788.36504 (S_0) -788.37234 (S_1) -788.25610 (S_2) -788.25964 (S_3)
S_1-81deg ($S_0 \rightarrow S_1$)	MM: -0.01661	
S_1-81deg ($S_0 \rightarrow S_2$)		

[a] For the abbreviations see text

[b] S_0-Z-1 corresponds to the FC structure

[c] S_0-E-1 corresponds to the FC structure

d The fixed solvent shell refers to the solvent shell structure at the Franck-Condon point

2.1 Z to E Initial Intrinsic Reaction Coordinate (IRC)

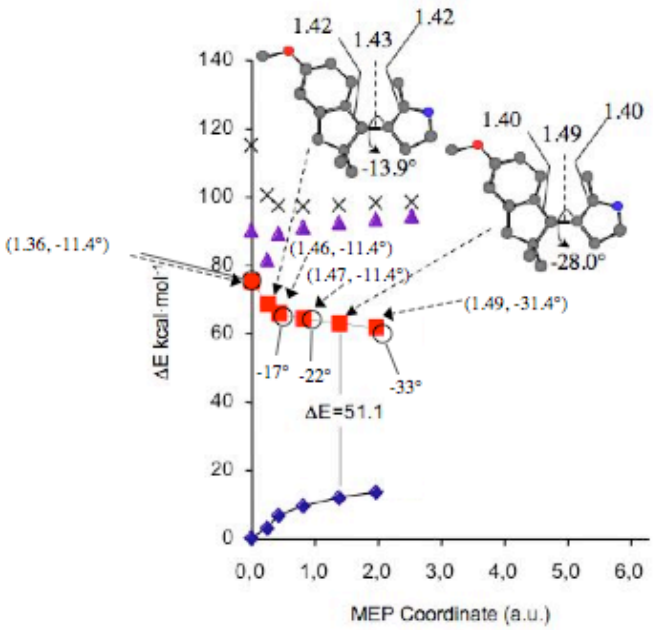

Figure S2.1 Initial part of an IRC computation (the point at 0.0 a.u. is the Franck-Condon point with torsional deformation -11.4º and corresponding to structure S_0-Z-**1**) for the Z→E S_1 photoisomerization path. Full diamonds, squares, triangles and crosses show the S_0, S_1, S_2, and S_3 CASPT2 energy profiles computed along the IRC coordinate. The structures and values in parenthesis (for the $C_{1'}$-C_4 central bond length and $C_{9'}$-$C_{1'}$-C_4-C_5 dihedral angle respectively) document the molecular changes along the reaction coordinate. The open circles indicate the energy of the scan points given in Fig. 1 of the main text which are closer (in terms of the value of the $C_{9'}$-$C_{1'}$-C_4-C_5 dihedral angle) to the computed IRC points. The geometrical parameters are given in Å and degrees.

3. E-CI-1 (-106°) to Z path

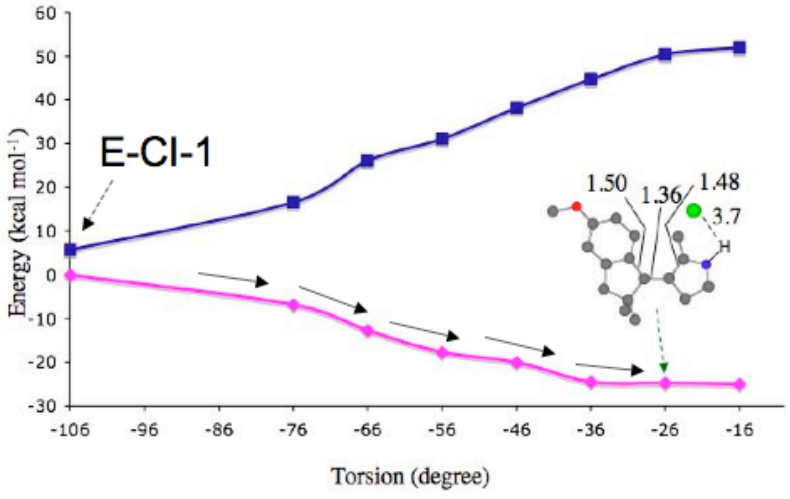

Figure S3.1: S_0 (lower curve) and S_1 (upper curve) energy profile for the E-CI-**1** to Z-**1** S_0 reaction path (solvent fixed) from single point 4-roots CASPT2//CASSCF/Amber computations. The energies are relative to E-CI-**1**. The geometrical parameters are given in Å and degrees. The solvent shell is unrelaxed.

4. The ASEP/MD Calculation of the E/Z equilibrium

4.1 Methodology

The ASEP/MD method has been used in the study of the vertical transitions energies for both the E and Z isomers and in the calculation of the in solution free energy difference between them.

ASEP/MD is a QM/MM effective Hamiltonian method that makes use of the mean field approximation(8), that is, it introduces into the solute molecular Hamiltonian the averaged perturbation generated by the solvent. The method combines quantum mechanics (QM) and molecular mechanics (MM) techniques, with the particularity that full QM and MM calculations are alternated and not simultaneous. During the MD simulations, the intramolecular geometry and charge distribution of all the molecules are considered as fixed. From the resulting data, the average electrostatic potential generated by the solvent on the solute is obtained. This potential is introduced as a perturbation into the solute's quantum mechanical Hamiltonian, and by solving the associated Schrödinger equation, one gets a new charge distribution for the solute, which is used in the next MD simulation. The iterative process is repeated until the electron charge distribution of the solute and the solvent structure around it are mutually equilibrated. The main characteristics of the method have been described elsewhere (8-12). Here, we shall detail only some points pertinent to the current study.

a) Geometry optimization

The solute geometry in presence of the solvent was optimized using a technique described in a previous paper (13)} and based on the use of the free-energy gradient method (14-16). At each step of the optimization procedure the mean value of total force, *F*, and the hessian, *H*, of the solute averaged over a representative set of solvent configurations were calculated as the sum of the solute and solvent contributions and were used to obtain a new geometry by using the Rational Function Optimization method. The force and Hessian read(13):

$$F(r) = -\frac{\partial G(r)}{\partial r} = -\left\langle \frac{\partial V(r,X)}{\partial r} \right\rangle \approx -\frac{\partial \langle V(r,X) \rangle}{\partial r} \qquad \text{[S4.1]}$$

$$H(r,r') \approx \frac{\partial^2 \langle V(r,X) \rangle}{\partial r \partial r'} \qquad \text{[S4.2]}$$

where G(r) is the free-energy, *V(r,X)* is a potential energy, sum of intra- and intermolecular (solute-solvent) contributions, and the brackets denote a statistical average over the solvent configurations, *X*.

b) Vertical transition energies

The determination of vertical transition energies with ASEP/MD involves two processes. In the first, the solvent structure and the charge distribution and geometry of the solute become mutually equilibrated. In the second, transition energies are calculated using the solvent structure and solute geometry obtained in the first step. During the electron transition we apply the Franck-Condon principle, hence, we consider as fixed the solute geometry and the solvent structure around it.

c) Free energy difference

Once the in solution structures of the "i" and "f" states have been determined, the standard free-energy difference between them can be written as sum of two terms

$$\Delta G_{diff} = \Delta E_{solute} + \Delta G_{\text{int}} \qquad \text{[S4.3]}$$

where

$$\Delta E_{solute} = E^f - E^i = <\psi^f | \hat{H}_{QM} | \psi^f > - <\psi^i | \hat{H}_{QM} | \psi^i > \qquad \text{[S4.4]}$$

is the *ab initio* difference between the two quantum mechanics, QM, states (excited and ground state in this case) calculated using the in vacuo solute molecular Hamiltonian, $\hat{H}_{QM}$, and the electronic wave-functions obtained in solution by solving the following Schrödinger equation

$$(\hat{H}_{QM} + \hat{H}^{elect}_{QM/MM}) | \psi >= E | \psi > \qquad \text{[S4.5]}$$

$$\hat{H}^{elect}_{QM/MM} = \int dr \cdot \hat{\rho} \cdot V_{ASEP}(r) \qquad \text{[S4.6]}$$

where V_{ASEP}(r) is the averaged electrostatic potential generated by the solvent, that in general depends on the solute state. Details about the calculation of $V_{ASEP}(r)$ can be found elsewhere(8-12). $\hat{\rho}$ is the charge density operator of the solute. The solute-solvent Lennard-Jones contribution is added to the energy a posteriori and hence has not effect on the solute wavefunction, obviously, it contributes to the final value of the gradient and Hessian.

In Eq. S4.3, ΔG_{int} is the difference in the solute-solvent interaction free energy between the two QM states. This term can be calculated by using the Free Energy Perturbation (FEP) method (17-19). The solute geometry was assumed to be rigid and a function of the perturbation parameter (λ) while the solvent was allowed to move freely. When $\lambda = 0$, the solute geometry, the charges and the solute-solvent Lennard-Jones parameters correspond to the initial state. When $\lambda = 1$, the charges, Lennard-Jones parameters, and geometry are those of the final state.

For intermediate values a linear interpolation is applied. The free-energy difference between the states at λ and λ + Δλ calculated through FEP theory is

$$\Delta G_{\lambda} = -RT\left\langle \exp\left(-\frac{\hat{H}_{QM/MM}(\lambda+\Delta\lambda)-\hat{H}_{QM/MM}(\lambda)}{RT}\right)\right\rangle_{\lambda} \qquad \text{[S4.7]}$$

where R is the gas constant, T is the absolute temperature and $\langle\rangle_k$ denotes the ensemble average at state λ. The total free-energy change between the two QM states is thus

$$\Delta G_{\text{int}} = \sum_{\lambda=0}^{\lambda=1} \Delta G_{\lambda} \qquad \text{[S4.8]}$$

A value of Δλ = 0.025 was used. That means that a total of 40 separate molecular dynamics simulations were carried out to determine the free energy. To test the convergence of the calculation, the differences in interaction free energy calculated forward and backward are compared.

The MD simulations were carried out using the program MOLDY (20). This program considers the system to be an assemblage of rigid molecules, and employs a modification of the Beeman algorithm proposed by Refson (21). The simulation had one chromophore molecule and 500 methanol molecules contained at fixed intramolecular geometry in a cubic box of 32.5 Å. No counterion was included. Previous studies of Rajamani and Gao (22) and Röhrig et al. (23) using chloride as counterion find that, because of the large dielectric screening effects of methanol, the effect of the counterion on the structure and spectra of the solute is minimal. This has been corroborated by experiments showing that the position of the chromophore absorption band in polar solvents is not affected by the nature of the counterion(24). The solute parameters were obtained by combining Lennard-Jones interatomic interactions (25) with electrostatic interactions. Periodic boundary conditions were applied, and spherical cutoffs were used to truncate the interaction between the solute and methanol at 12 Å. The electrostatic interaction was calculated with the Ewald method. The temperature was fixed at 298 K using the Nosé-Hoover (26) thermostat. Each simulation was run for 150 000 time steps, where 50 000 were for equilibration and 100 000 for production. A time step of 0.5 fs was used.

4.2 Results

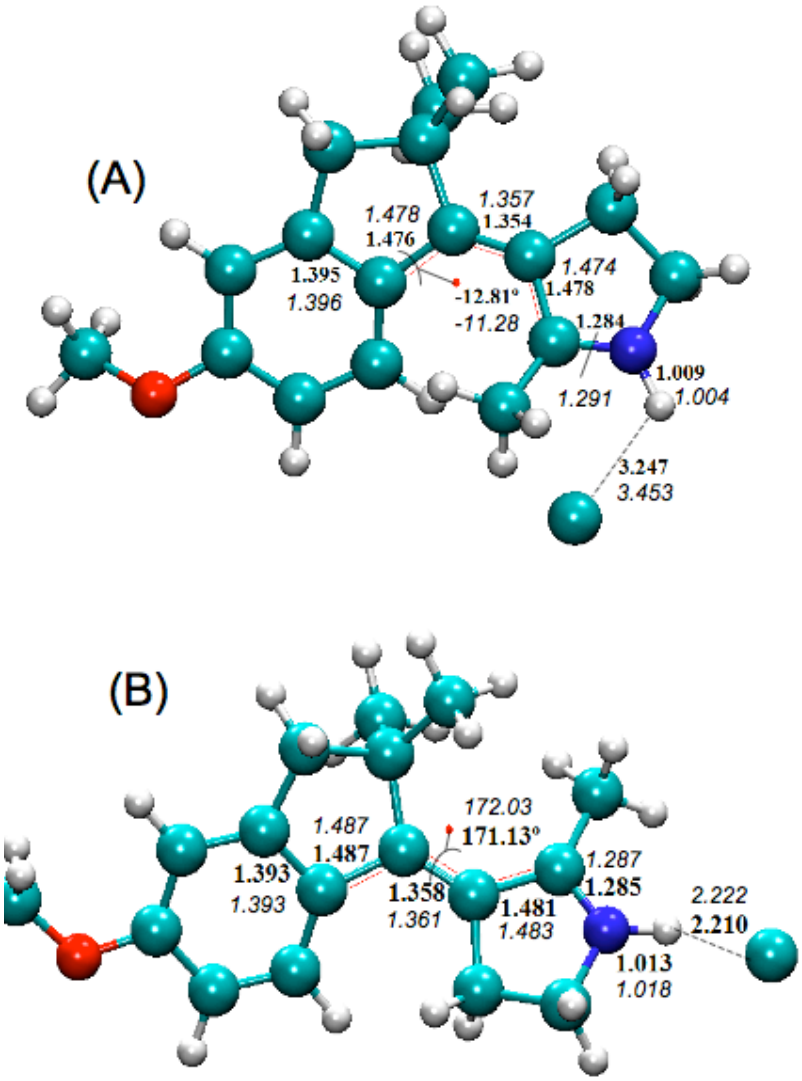

Figure S4.1: Comparison between the S_0 equilibrium structures computed with the ASEP/MD solvent model and the approximate solvent model described in Section 1 (parameters in *italics*). (A) S_0-Z-**1** and (B) S_0-E-**1** The geometrical parameters are given in Å and degrees.

Table S4.1 Lennard-Jones solute-solvent interaction parameters.

	R* (Å)	***ε(kcal/mol)***
Methanol		
O	1.7210	0.2104
C	1.9080	0.0860
H	1.4870	0.0157
H(OH)	0.0000	0.0000
Solute		

C(sp3)	1.8891	0.1094
C(sp2)	1.8778	0.0860
N	1.8311	0.1700
H(NH)	0.6024	0.0157
O	1.6837	0.1700
Cl	2.4700	0.1000

Table S4.2 Energies for Z-**1** and E-**1** isomers where both Z and Cl- are considered as quantum particles (See text for details)

Z-1		S_0	S_1	S_2	S_3
CASPT2 (hartree)	Cycle 16	-1248.12352	-1248.00027	-1247.97383	-1247.93477
	Cycle 17	-1248.13068	-1248.00544	-1247.97999	-1247.94246
	Cycle 18	-1248.11670	-1247.99416	-1247.96746	-1247.93097
	Cycle 19	-1248.11715	-1247.99364	-1247.96729	-1247.93073
	Cycle 20				
			$S_0 \rightarrow S_1$	$S_0 \rightarrow S_2$	$S_0 \rightarrow S_3$
ΔE (kcal mol^{-1})	Cycle 16	-	77.3391	93.9301	118.4417
	Cycle 17	-	78.5889	94.5541	118.1057
	Cycle 18	-	76.8941	93.6488	116.5518
	Cycle 19	-	77.5027	94.0339	116.9756
	Cycle 20	-	77.4938	94.2864	116.2122
Average value		-	77.564±0-62	94.091±0.35	117.257±0.97

E-1		S_0	S_1	S_2	S_3
CASPT2 (hartree)	Cycle 11	-1248.20023	-1248.07303	-1248.04929	-1248.01477
	Cycle 12	-1248.21558	-1248.08698	-1248.06427	-1248.03102
	Cycle 13	-1248.21811	-1248.09225	-1248.06792	-1248.03164
	Cycle 14	-1248.20530	-1248.07820	-1248.05436	-1248.01927
	Cycle 15	-1248.20621	-1248.07801	-1248.05493	-1248.02059
			$S_0 \rightarrow S_1$	$S_0 \rightarrow S_2$	$S_0 \rightarrow S_3$
ΔE (kcal mol^{-1})	Cycle 11	-	79.8171	94.7174	116.3755
	Cycle 12	-	80.6980	94.9433	115.8122
	Cycle 13	-	78.9749	94.2475	117.0085
	Cycle 14	-	79.7532	94.7146	116.7347
	Cycle 15	-	80.4465	94.9268	116.4744
Average value		-	79.94±0.67	94.71±0.28	116.48±0.45

Table S4.3 Free energy calculation.

	Internal energy[a] (ua)	
	Z Isomer	***E Isomer***
Cycle 11	-785.783425	-785.778818
Cycle 12	-785.782779	-785.780372
Cycle 13	-785.783346	-785.779725
Cycle 14	-785.782805	-785.779569
Cycle 15	-785.782859	-785.781224
Average	-785.783043	-785.779942
SD[b] (kcal mol^{-1})	0.1979	0.5681

[a] $E = <\psi \mid \hat{H}^0{}_{QM} \mid \psi>$

[b] Standard deviation

According to equation S4.3

$$\Delta G_{diff} = \Delta E_{solute} + \Delta G_{\text{int}} = <\psi^Z \mid \hat{H}^0{}_{QM} \mid \psi^Z> - <\psi^E \mid \hat{H}^0{}_{QM} \mid \psi^E> + \Delta G_{\text{int}} =$$

$$-1.9462298 + 1.22427208 = -0.722 \text{ kcal mol}^{-1}$$

where ΔG_{int}, the difference in the solute-solvent interaction free energy between the two QM states, has been calculated by using the Free Energy Perturbation (FEP) method.

5. A 2D model for the initial photoexcited dynamics.

We adopted a two-dimensional (2D) model for the potential energy surface (PES) of the S_1 excited-state of the chloride--Z-**1** ion pair in solution. The two coordinates are respectively a stretching x of the conjugated carbon backbone and the -C1'=C4- reactive torsion φ. The 2D potential is plotted in Fig. S9-1 where the blue spot indicates the FC point, i.e. the position of the minimum of the ground electronic state S_0.

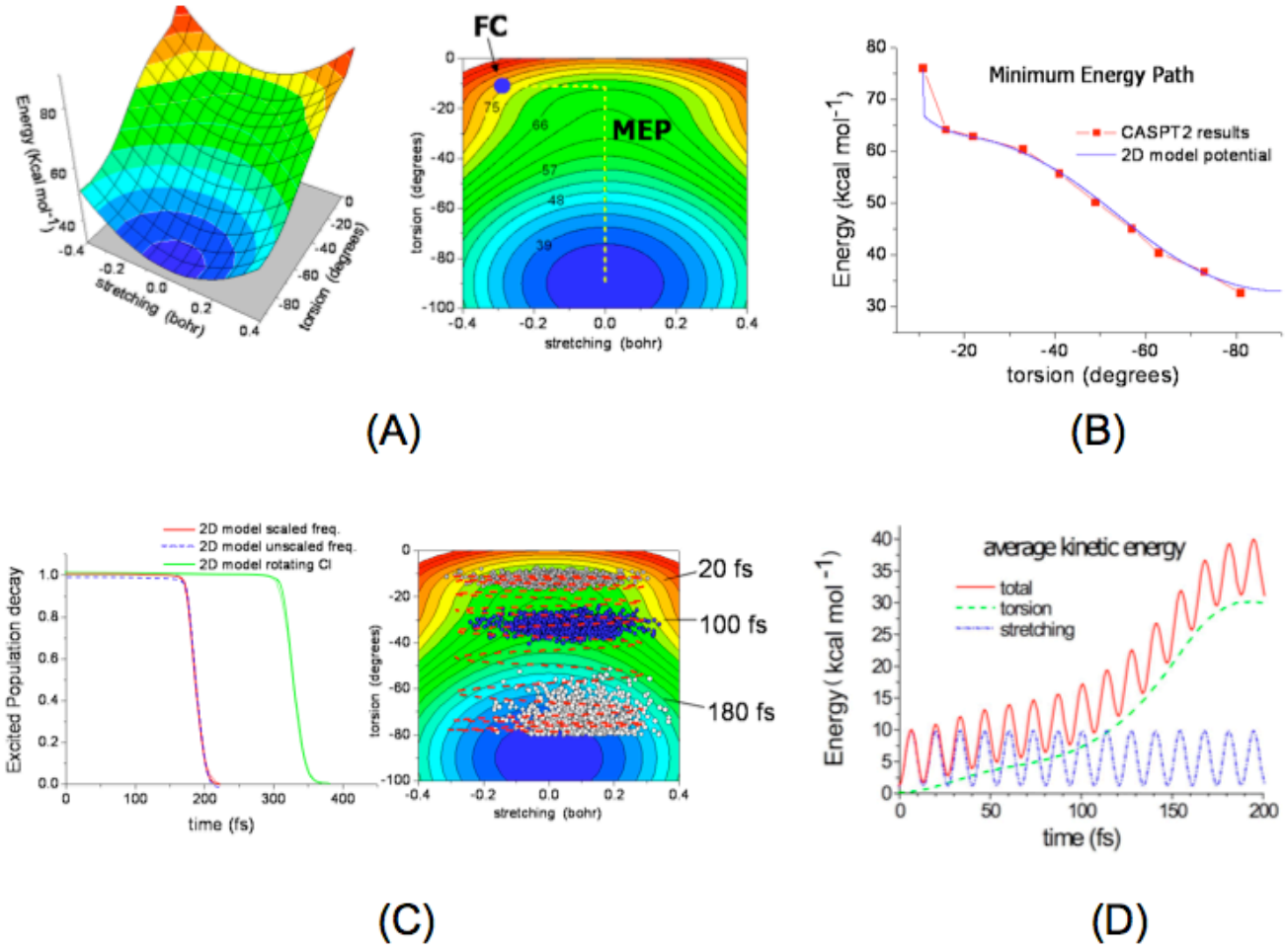

Figure S5.1: Formulation of the S_1 potential energy surface 2D-model. (A) 3D Plot (left) and contour plot (right) of the 2D model $V_1(x,\varphi)$ of the S1 PES of chloride•Z-**1** chromofore in solution (the yellow line reports pictorially the minimum energy path). (B) Minimum energy path as function of the reactive torsion, computed for the real molecule in full-coordinate space at the CASPT2 level and for the 2D model potential. (C) Left panel: decay of the excited state population for the 2D model with scaled frequencies and frozen position for Cl anion (red curve), with unscaled frequencies and frozen position for Cl anion (blue curve), and with scaled frequencies and Cl^- rotating with the pirroline ring (green curve). Right panel: average position

of the wavepacket as a function of time (red dashed curve), and three snapshots of the wavepacket at 20 fs (gray spots), 100 fs (blue spots), and 180 fs (white spots); in background the contour plot of the 2D potential. (D) Kinetic energy time evolution for the 2D model, scaled frequencies, moment of inertia computed for Chlorine fixed in space (faster model). At longer times the average kinetic energy is not meaningful anymore.

The 2D potential $V_1(x,\varphi)$ reproduces all the known features of the S_1 PES of chlorine--Z-**1,** and in particular its MEP closely resembles the CASPT2//CASSCF MEP (see Fig. S9-2). Details on the mathematical expression of $V_1(x,\varphi)$ are postponed to the next section. The **FC** point is at φ=-11 degrees, with an energy of 75.9 Kcal mol^{-1}. At the increase of the twisting φ the potential shows up a quasi-plateau in the region -33<φ<-16 and then the energy decreases steeper with φ, being 36.4 Kcal mol^{-1} at φ=-73 degrees and x=0. At smaller values of the torsion coordinate (i.e. moving toward a perpendicular arrangement) the MEP on the S_1 surface of the true molecule enters into an intersection seam **CI** with the ground state S_0 (see Fig. 2 of the text).

The present 2D model is designed to describe the motion of the initial wavepacket starting in the **FC** region toward the **CI** region, assuming that once reached **CI** it never goes back to **FC.** As the model does not explicitly describe the nonadiabatic transition S_1/S_0, the exact shape of the potential in the region of the perpendicular arrangements is not relevant, and the intersection seam is conveniently substituted by a global minimum, named by analogy **CI**, located at x=0 and φ=-90 lying at 33 Kcal mol^{-1}. The ground state potential is assumed to be harmonic, with parameters indicated in the next section. The excited state potential energy surface is harmonic with respect to x but not to φ. The model assumes, consistently with the result of trajectory simulations on Rhodopsin (see ref. 32 in the main text), that a negligible amount of kinetic energy could be transfer between the two modes within the excited state lifetime.

5.2 Mathematical expression for the 2D model of the S_0 and S_1 PES.

The PES of the ground electronic state S_0 is harmonic

$$V_0(x,\varphi) = V_{x0}(x) + V_{\varphi 0}(\varphi) \qquad [S5.1]$$

$$V_{x0}(x) = \frac{1}{2}\mu_x\omega_{x0}^2(x-x_{FC})^2 \quad \text{and} \quad V_{\varphi 0}(y) = \frac{1}{2}I_\varphi\omega_{\varphi 0}^2(\varphi-\varphi_{FC})^2 \qquad [S5.2]$$

where the **FC** point is (x_{FC}, φ_{FC}), with $\varphi_{FC} = 11$ degrees and $x_{FC} = -0.2883$ bohr (this latter chosen to reproduce the CASPT2 **FC** energy). The mass associated to the stretching is 6 amu, i.e the reduced mass of a C-C stretching. The moment of inertia associated to the torsion has been obtained assuming a rigid rotation around the axis of the C1'-C4 bond of both the left (moment of inertia I_L) and the right (moment of inertia I_R) moieties of the molecule and computing the reduced moment $I_\varphi = I_L I_R / (I_L + I_R)$. The chlorine counterion has been excluded from the computation, considering that it does not follow adiabatically the twisting. This choice is justified by the fact that it is not connected to the solute molecule by covalent bonds but only through coulombian and not directional forces, and that being rather heavy it should have a larger inertia to motion. The resulting value for I_φ is 572 amu bohr^2.

To choose the frequencies of the two modes, we performed a CASSCF(10,9)/3-21G* normal mode analysis of the S_0 minimum. The frequency associated to the reactive torsion is 131.5 cm^{-1}, while we identified two normal modes, with frequency 1739.8 cm^{-1} and 1764.6 cm^{-1} respectively, that contribute significantly to the backbone stretching *x* leading from the **FC** point toward **CI**. Therefore we associated to *x* a frequency with the average value 1752.2 cm^{-1}. CASSCF frequencies are often scaled by an empirical factor 0.9 to take into account the lack of the effect of dynamical correlation. In conclusion we used the values ω_{x0} =1577 cm^{-1} for the stretching and $\omega_{\varphi 0}$ =124 cm^{-1} for the torsion, checking that, as we will comment below, our results are negligibly dependent on their exact values (obviously, if they vary in a reasonable range).

The mathematical expression of the S_1 PES is still harmonic along the stretching *x* but more complex along φ so to describe the plateau region. The parabola along *x* has a minimum at $x = 0$

$$V_1(x,\varphi) = V_{1x}(x) + V_{1\varphi}(\varphi) \qquad V_{1x}(x) = 1/2\mu_x\omega_x^2 x^2 \qquad \text{[S5.3]}$$

To establish the value of the frequency ω_x we performed an excited-state CASSCF(10,9)/3-21G* normal mode analysis for the structure corresponding to a -16 degrees twisting around of the C1'-C4 bond, corresponding to the quasi-minimum on the excited-state MEP reported in Figure. SI5.1B. As in the ground state case, there are two normal modes that contribute

significantly to our model *x* stretch, with frequencies of 1368.1 cm^{-1} and 1390.5 cm^{-1} . The average frequency is 1379.3 which once scaled by the usual 0.9 factor gives a value ω_x = 1241 cm^{-1}.

Mimicking the ab initio data the S_1 profile along the torsion φ is more complex. Briefly, it is expressed as the lower PES deriving from the coupling of two parabola with different equilibrium positions.

$$V_a(\varphi) = 1/2 I_\varphi \omega_a^2 (\varphi - \varphi_{0a})^2 + E_0 \qquad \text{[S5.4]}$$

$$V_b(\varphi) = 1/2 I_\varphi \omega_b^2 (\varphi - \varphi_{0b})^2 \qquad \text{[S5.5]}$$

$$V_c(y) = c \exp(-(\varphi - \varphi_c)^2 / \gamma^2) \qquad \text{[S5.6]}$$

$$V_{l\varphi}(\varphi) = \frac{V_a(\varphi) + V_b(\varphi)}{2} - \sqrt{\frac{(V_a(\varphi) - V_b(\varphi))^2}{4} + V_c^2(\varphi)} \qquad \text{[S5.7]}$$

This expression allows to create a flexible double-minimum shape with variable barrier (or plateau) and equilibrium positions. The values of the parameters ω_a =170 cm^{-1} , $\omega_b = \omega_a / \sqrt{5}$, φ_{0a} =-16 degrees, φ_{0b} =-90 degrees, E_0 =31 Kcal/mol, φ_c =-36 degrees, *c*=17 Kcal/mol and γ =23 degrees allow to reproduce the minimum energy path on the S_1 surface of the full-dimensionality system Z-**1** as computed at CASPT2//CASSCF level (see Fig. S5.1B).

5.3 Results.

We simulate the motion of an initial wavepacket prepared by an ultrafast excitation of the ground vibrational state $|g\rangle$ of the S_0 PES, running a bunch of 1000 trajectories whose initial conditions sample the Wigner distribution of $|g\rangle$ (both in the coordinate and in the momenta space), and we computed the decay of the excited population $P(t)$ toward the conical intersection **CI** as $1 - N(t)$, where $N(t)$ is the percent of trajectories that reach the border φ =-80 degrees (approximately where the intersection seam meets the MEP in the real molecule, see Fig. 1 of the text. Here the trajectories are assumed to make a transition to S_0 and therefore to disappear from S_1.

The results of our calculations are reported in Fig. SI5.1C. The red curve in the left panel shows the decay of the excited state population. After an induction time of about 160 fs, the trajectories start crossing the border φ=-80 degrees, reaching the region of the intersection seam **CI**. The excited population is reduced to 0.5 in 189 fs, and the decay is completed in 225 fs. The right panel of Fig. S5.1C reports the wavepacket average position (red dashed line), and snapshots of the wavepacket (plotted as an ensemble of spots, each indicating the position of a different trajectory of the bunch) at three different times *t*=20 fs, *t*=100 fs and *t*=180 fs. It is clearly seen that the wavepacket experiences several oscillations along the stretching coordinate while progressively moving along the torsion toward the global minimum region **CI**. Notice that at 180 fs already 25% of the trajectories have crossed the φ=-80 degrees border, and therefore they have been removed from the simulation.

In conclusion the 2D model potential suggests a $\approx$200 fs timescale for the excited state population decay, in remarkable agreement with the experimental findings. Our results are only negligibly dependent on the exact choice of the model parameters. For example, the decay is unaltered if we do not scale the CASSCF frequencies (see next section), i.e using ω_{x0} =1752.2 cm^{-1}, $\omega_{\varphi 0}$ =131.47 cm^{-1} and ω_x =1379.3 cm^{-1} (see blue curve in figure S5.1C). The decay is more dependent on the choice to exclude the Cl anion in the computation of the reduced moment of inertia I_φ, since it is rather heavy and its distance from the rotation axis is more than 10 bohr. To obtain an upper limit for the decay timescale, we repeated the calculation assuming that Cl$^-$ rotates together with the pirroline ring, the choice leading to the largest value for I_φ. In that case the excited population is reduced to 0.5 in about 320 fs (see green curve in figure S5.1C), still in reasonable agreement with the experiments.

6. Spectroscopic Measurements

6.1 Fs fluorescence set-up

The experimental set-up is described in detail in ref. (27, 28). Briefly, the sample is excited at 400 nm by means of pulses with a typical width of 80 fs, a power of 10 nJ/pulse, a focal spot of 30 μm (FWHM) and a repetition rate of 100 kHz. A temporal resolution of ca. 120 fs (FWHM) is achieved. The sample was flown in a 0.5 mm thick quartz flow cell at a speed of ca. 5 m/s to avoid photodegradation and multiple excitations. Indeed with the above experimental conditions, the 400 nm pulse hits the same spot ~1 time. The luminescence, collected in forward scattering geometry, is up-converted in a 250 μm thick beta barium borate (BBO) crystal by mixing with a pulse at 800 nm (Gate). The up-converted signal is spatially filtered and detected with a spectrograph and a liquid-N_2 cooled CCD camera in polychromatic mode (27, 29). Schott filters GG420 and UG-11 are used to attenuate the remaining 400 and 800 nm light. This greatly improves the signal-to-noise ratio but it limits the detectable spectral range to the 440-690 nm region. The collected luminescence signal was corrected for the Group Velocity Dispersion (GVD) over the entire detection range (the blue-most component is delayed by ~400 fs with respect to the red-most one). The GVD was measured by recording a white light pulse signal generated in a neat water solution under the same experimental conditions. To determine the time zero *in situ*, we analyzed the region around 457 nm, where the solvent Raman line is expected.

6.2 UV/Vis pump-probe experiment and data processing

For the UV/VIS pump-probe experiments, a commercial 5 kHz Ti:Sapphire amplified laser system (Pulsar, Amplitude Technologies) was used delivering ~40 fs pulses at 800 nm. UV-pump pulses at 400 nm were obtained by SHG in a 0.2 mm BBO crystal, and the white-light probe pulses were generated in a 1.5 mm CaF_2 plate. Probe and reference beams were recorded at a 220 Hz rate with a spectrograph/CCD combination covering 300 nm spectral range with 2.8 nm resolution. The data presented have been measured in two subsequent runs, addressing the near-UV and VIS portions separately. For the VIS part a Schott OG 420 was mounted after the flow cell to reduce scattered 400 nm light. The chirp of the probe beam was determined via the "coherent artifact" in the flow cell quartz windows, measured in a separate experiment in the absence of photoswitches. The group velocity delay was minimized (< 300 fs over the entire

300 nm band width) by eliminating dispersive elements in the beam path between the sapphire crystal and the flow cell. The data presented are corrected for group velocity delay and the cross-phase modulation effects. In the raw data, the latter are comparable to the photoswitch-related signal only for wavelengths < 480 nm. The instrument response function has a FWHM of 90 fs at 450 nm. The exc. density is low enough (on the order of 0.1 mJ/cm^2 per pulse) to observe the pump-induced absorption increasing linearly with the pump power. The pump beam polarization was set at magic angle to the main axis of polarization of the probe beam. An absorption spectrum of the sample taken immediately after the time-resolved measurements shows formation of < 2% of the E isomer and a negligible signature of photo-alteration at wavelengths < 250 nm.

The kinetic traces of both fluorescence and pump-probe data are analyzed by a sum of exponential functions multiplied by Heavyside step functions H(t-t_0) centered on the signal onset time t_0, and followed by a convolution with the instrument response function assumed to be Gaussian.

$$S(t) = \sum_i H_i(t - t_0^i) A_i e^{-t/\tau_i} \otimes e^{-0.5\left(\frac{t}{\sigma}\right)^2} \qquad [S6.1]$$

For the fluorescence data, a "global" fit approach has been applied, in which the two decay times τ_1 and τ_2 are assumed to be wavelength-independent, while only the amplitudes A_i are allowed to change. The rise and decay times found for the transient absorption are given in the text. We note that the SE and ESA start with $t_0 \sim 0$, while the IA and hot GSA signals are found to be significantly delayed with wavelength-dependent t_0 = 0.2-0.3 ps. The relation between this delay and the isomerization time (formation of E) is discussed in the text.

6.3 Mid-IR pump-probe experiments

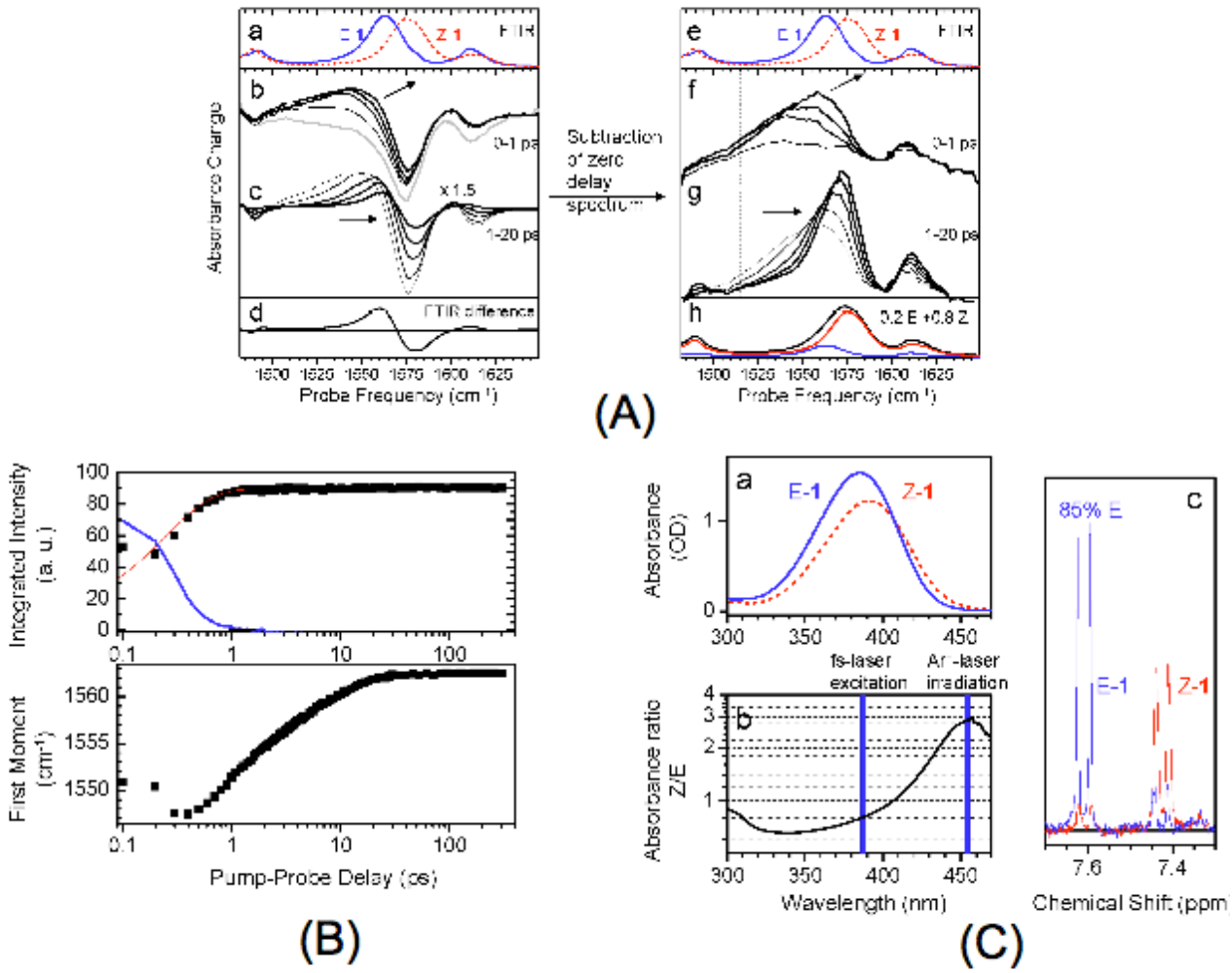

Figure S6.1: Mid-IR data. (A) Mid-IR pump-probe data before (panels b and c) and after (panels f and g) subtraction of the transient spectrum at delay 0 (grey line in panel b). Although the two sets of data are identical, the right hand representation better reflects the growth and time-dependent band shift of E and Z bands after photoexcitation. (B) The upper panel shows the integrated band intensity (solid squares) of the mid-IR absorption signal in panels f and g of Figs. S6.1A, reflecting the return of the excited population to the electronic ground state on a sub-picosecond timescale. The red line is an exponential fit with a 300 fs time constant. The blue line shows the time-dependent baseline offset of the data in Figs. 5 (main text) and S6.1A, which has been subtracted prior to analysis. The lower panel shows the first moment of the same set of data, reflecting the band shift as a result of solvation and dissipation of the excess energy to the solvent on a picosecond timescale. The integration limits are indicated by vertical dashed lines in Fig. S6.1A. (C) Panel a: NMR-calibrated UV/vis absorption spectra of Me-Z-**1** and Me-E-**1**. Panel b: ratio of the absorption bands of part a, showing the possibility of enhancing the E-population by continuous irradiation at 454.5 nm (Ar+-laser line) and subsequent selective excitation of the E conformer at 388 nm. Panel c: 300 MHz ^{1}H-NMR spectra of the sample used

in the mid-IR experiments in the photostationary state upon irradiation at 454.5 nm (blue line, ca. 85% E) and before irradiation (red line).

Femtosecond light pulses for transient IR spectroscopy were obtained from a commercial Ti:Sapphire amplified laser system (Spectra Physics), tunable near 800 nm (duration ~100 fs, repetition rate 1 kHz, energy ~800 μJ/pulse). UV-pump pulses at 420 nm or 388 nm were obtained by frequency–doubling in a 500 mm BBO crystal. The mid-IR pulses centered near 6000 nm (1.5 mJ, 100 fs) were produced by frequency mixing the signal and idler output of a home-built two–stage BBO optical parametric amplifier (OPA) in an $AgGaS_2$ crystal (30). A small fraction of the IR light was split off and focused onto the sample cell in spatial overlap with the UV-pump pulses. A second fraction was used as a reference beam and passed the sample cell approximately 0.5 mm upstream. Spectra for Z-excitation (Fig. 4 in the main text) were recorded on a 64 pixel double MCT array detector (probe and reference beam) with parallel and perpendicular polarizations of the 420 nm pump and the mid-IR probe pulses, from which a magic angle signal was calculated. The nominal resolution (difference between two pixels) was 2 cm^{-1} at 1600cm^{-1}. Water vapor was used for spectral calibration and for the exact matching of data recorded in different spectral windows. The time resolution of the experiment was determined from the rise time of the UV-induced absorption signal of a germanium crystal, yielding approximately 300 fs. The transient IR-spectra for 388 nm excitation of the Z and E form (Fig. 5) were recorded using a 32 pixel detector (4 cm^{-1} resolution) in an otherwise identical setup.

Growth and shift of the photoproduct bands are better seen after subtracting from all subsequent signals the transient spectrum at zero time delay. This subtraction yields the 'true' time-dependent absorption spectrum of those molecules that have absorbed a UV photon (Compare panel a and b in Figs. S6.1A).

The time evolution of the integrated band intensity (integration limits are indicated by the vertical lines in Fig. S6.1A) are shown by solid squares in Fig. S6.1Ba. The integrated intensity of the C=C stretch band is almost completely recovered on a timescale of a few hundred femtoseconds. A fit to the data indicates a 300 fs rise time (red line), however, this number should be considered with caution because a time-dependent baseline (taken as the signal at 1645 cm^{-1}) has been subtracted from the data, and this background varies on a

comparable timescale (blue line in Fig. S6.1Ba). It may be tentatively assigned to a strongly broadened excited state signal with additional contributions from the Kerr effect. Despite this uncertainty, the ultrafast appearance of the photoproduct band is clearly evident from the spectral changes in Figs. 5 (main text) and S6.1A, indicating that isomerization takes place in less than 1 ps. The first moment of the spectra in panels f and g of Figs. S6.1A, which is displayed in panel b of Fig S6.1B, is a measure for the time-dependent band shift. It is caused by anharmonic coupling of the C=C stretch vibration to low frequency modes that get excited by the excess photon energy. The band shift also shows an ultrafast, sub-picosecond component. However, the main shift takes place on a timescale of 6-9 ps, when only very small changes in band intensity are observed. This shift reflects the heat dissipation from the molecule to the solvent in the electronic ground state after isomerization is completed, as well as solvation.

6.4 Accumulation of the E-form

In order to study the E→Z back reaction, we used an additional Ar-Ion laser beam (200mW) to continuously irradiate the sample at 454.5 nm, where the Z absorption is approximately three times stronger than that of E. ^{1}H-NMR analysis showed that this transferred 85-90 % of the molecules to the E-form.

References

1. Case D A, Pearlman, D. A., Caldwell, J. W., Cheatham III, T. E., Wang, J., Ross, W. S., Simmerling, C. L., Darden, T. A., Merz, K. M., Stanton, R. V., Cheng, A.L., Vincent, J. J., Crowley, M., Tsui, V., Gohlke, H. Radmer, R. J., Duan, Y., Pitera, J., Massova, I., Seibel, G. L., Singh, U. C., Weiner, P. K., Kollman, P. A. (2002) (University of California, San Francisco).
2. Frisch M J, Trucks G W, Schlegel H B, Scuseria G E, Robb M A, Cheeseman J R, J. A. Montgomery J, Vreven T, Kudin K N, Burant J C, Millam J M, Iyengar S S, Tomasi J, Barone V, Mennucci B, Cossi M, Scalmani G, Rega N, Petersson G A, Nakatsuji H, Hada M, Ehara M, Toyota K, Fukuda R, Hasegawa J, Ishida M, Nakajima T, Honda Y, Kitao O, Nakai H, Klene M, Li X, Knox J E, Hratchian H P, Cross J B, Adamo C, Jaramillo J, Gomperts R, Stratmann R E, Yazyev O, Austin A J, Cammi R, Pomelli C, Ochterski J W, Ayala P Y, Morokuma K, Voth G A, Salvador P, Dannenberg J J, Zakrzewski V G, Dapprich S, Daniels A D, Strain M C, Farkas O, Malick D K, Rabuck A D, Raghavachari K, Foresman J B, Ortiz J V, Cui Q, Baboul A G, Clifford S, Cioslowski J, Stefanov B B, Liu G, Liashenko A, Piskorz P, Komaromi I, Martin R L, Fox D J, Keith T, Al-Laham M A, Peng C Y, Nanayakkara A, Challacombe M, Gill P M

W, Johnson B, Chen W, Wong M W, Gonzalez C & Pople J A (2003) (Gaussian, Inc., Pittsburgh PA).
3. Andruniow T, Fantacci S, Angelis F D, Ferré N & Olivucci M (2005) Mechanism of the initial conformational transition of a photomodulable peptide *Angew Chem Int Ed* 44:6077-6081.
4. Ferré N, Cembran A, Garavelli M & Olivucci M (2004) Complete-active-space self-consistent-field/Amber parameterization of the Lys296–retinal–Glu113 rhodopsin chromophore-counterion system *Theor Chem Acc* 112:335-341.
5. Wang J, Wolf R M, Caldwell J W, Kollman P A & Case D A (2004) Development and testing of a general amber force field *J Comp Chem* 25:1157-1174.
6. Ponder J W & Richards F M (1987) An efficient newton-like method for molecular mechanics energy minimization of large molecules *J Comp Chem* 8:1016-1024.
7. Andersson K, Barysz M, Bernhardsson A, Blomberg M R A, DCooper D L, Fülscher M P, Graaf C, Hess B A, Karlström G, Lindh R, Malmqvist P-A, Nakajima T, Neogrády P, Olsen J, Roos B O, Schimmelpfennin B, Schütz M, Seijo L, Serrano-Andrés L, Siegbahn P E M, Stålring J, Thorsteinsson T, Veryazov V & Widmark P-O (2002), Lund University, Sweden).
8. Sánchez M L, Martín M E, Fdez. Galván I, Olivares del Valle F J & Aguilar M A (2002) Theoretical Calculation of the Stark Component of the Solute-Solvent Interaction Energy. Validity of the Mean Field Approximation in the Study of Liquids and Solutions *J Phys Chem B* 106:4813-4817.
9. Sánchez M L, Aguilar M A & Olivares del Valle F J (1997) Study of solvent effects by means of averaged solvent electrostatic potentials obtained from molecular dynamics data *J Comp Chem* 18:313-322.
10. Sánchez M L, Martín M E & Aguilar M A O d V, F. J. (2000) Solvent effects by means of averaged solvent electrostatic potentials: Coupled method *J Comp Chem* 21:705-715.
11. Muñoz Losa A, Fdez. Galván I, Martín M E & Aguilar M A (2003) Theoretical Study of Liquid Hydrogen Fluoride. Application of the Averaged Solvent Electrostatic Potential/Molecular Dynamics Method *J Phys Chem B* 107:5043-5047.
12. Fdez. Galván I, Sánchez M L, Martín M E, Olivares del Valle F J & Aguilar M A (2003) ASEP/MD: A program for the calculation of solvent effects combining QM/MM methods and the mean field approximation *Comp Phys Commun* 155:244-259.
13. Fdez. Galván I, Sánchez M L, Martín M E, Olivares del Valle F J & Aguilar M A (2003) Geometry optimization of molecules in solution: Joint use of the mean field approximation and the free-energy gradient method *J Chem Phys* 118:255-263.
14. Okuyama-Yoshida N, Nagaoka M & Yamabe T (1998) Transition-state optimization on free energy surface: Toward solution chemical reaction ergodography *Int J Quantum Chem* 70:95-1003.
15. Okuyama-Yoshida N, Kataoka K, Nagaoka M & Yamabe T (2000) Structure optimization via free energy gradient method: Application to glycine zwitterion in aqueous solution *J Chem Phys* 2000:3519-3524.
16. Hirao H, Nagae Y & Nagaoka M (2001) Transition-state optimization by the free energy gradient method: Application to aqueous-phase Menshutkin reaction between ammonia and methyl chloride *Chem Phys Lett* 348:350-356.
17. Debolt S E & Kollman P A (1990) A theoretical examination of solvatochromism and solute-solvent structuring in simple alkyl carbonyl compounds. Simulations using statistical mechanical free energy perturbation methods. *J Am Chem Soc* 112:7515-7524.
18. Kollman P A (1993) Free energy calculations: Applications to chemical and biochemical phenomena *Chem Rev* 93:2395-2417.

19. Mark A E (1998) in *Encyclopedia of Computational Chemistry*, eds. Schleyer, P V R, N L Allinger, T Clark, J Gasteiger, P A Kollman, H F Schaefer III & P R Schreiner (Wiley and Sons, Chichester), pp. 1070-1083.
20. Refson K (2000) Moldy: a portable molecular dynamics simulation program for serial and parallel computers *Comp Phys Comm* 126:310-329.
21. Refson K (1985) Molecular dynamics simulation of solid n-butane *Physica B* 131:256-266.
22. Rajamani R & Gao J (2002) Combined QM/MM study of the opsin shift in bacteriorhodopsin *J Comp Chem* 23:96-105.
23. Röhrig U F, Guidoni L & Rothlisberger U (2005) Solvent and Protein Effects on the Structure and Dynamics of the Rhodopsin Chromophore *Chem Phys Chem* 6:1836-1847.
24. Blatz P E & Mohler J H (1975) Effect of selected anions and solvents on the electronic absorption, nuclear magnetic resonance, and infrared spectra of the N-retinylidenebutylammonium cation *Biochemistry* 14:2304-2309.
25. Cornell W D, Cieplack P, Bayly C I, Groud K M, Fergurson D M, Spellmeyer D C, Fox T, Cladwell J W & Kollman P A (1995) A Second Generation Force Field for the Simulation of Proteins, Nucleic Acids, and Organic Molecules *J Am Chem Soc* 117:5179-5197.
26. Hoover W G (1985) Canonical dynamics: Equilibrium phase-space distributions *Phys Rev A* 31:1695-1697.
27. Zgrablić G, Voïtchovsky K, Kindermann M, Haacke S & Chergui M (2005) Ultrafast Excited State Dynamics of the Protonated Schiff Base of All-trans Retinal in Solvents *Biophys J* 88:2779-2788.
28. Zgrablić G (2006) in *Laboratoire de spectroscopie ultrarapide* (Écoles Polytechniques Fédérales de Lausanne, Section de Physique, Lausanne), pp. 100.
29. Zhao L, Pérez Lustres J L, Farztdinov V & Ernsting N P (2005) Femtosecond fluorescence spectroscopy by upconversion with tilted gate pulses *Phys Chem Chem Phys* 7:1716-1725.
30. Hamm P, Kaindl R A & Stenger (2000) Noise suppression in femtosecond mid-infrared light sources *Opt Lett* 25:1798-1800.